

1 **3D tree dimensionality assessment using photogrammetry and small unmanned aerial vehicles**

2

3 Demetrios Gatziolis^{1,\$}, Jean F. Lienard^{2,\$}, Andre Vogs^{3,\$}, Nikolay S. Strigul^{2,\$,*}

4 ¹ - USDA Forest Service, Pacific Northwest Research Station, Portland, Oregon

5 ² - Department of Mathematics, Washington State University, Vancouver, Washington

6 ³ - Intel Inc., Hillsboro, OR, volunteer for WSU environmental robotics program

7 \$ - authors contributed equally

8 * - corresponding author email: nick.strigul@vancouver.wsu.edu

9 **Keywords:**

10 3D models, tree geometry, crown plasticity, individual-based forest models, photogrammetry, drones,
11 forest inventory

12

13 **Abstract**

14 Detailed, precise, three-dimensional (3D) representations of individual trees are a prerequisite for an
15 accurate assessment of tree competition, growth, and morphological plasticity. Until recently, our ability
16 to measure the dimensionality, spatial arrangement, shape of trees, and shape of tree components with
17 precision has been constrained by technological and logistical limitations and cost. Traditional methods
18 of forest biometrics provide only partial measurements and are labor intensive. Active remote
19 technologies such as LiDAR operated from airborne platforms provide only partial crown
20 reconstructions. The use of terrestrial LiDAR is laborious, has portability limitations and high cost. In this
21 work we capitalized on recent improvements in the capabilities and availability of small unmanned
22 aerial vehicles (UAVs), light and inexpensive cameras, and developed an affordable method for obtaining
23 precise and comprehensive 3D models of trees and small groups of trees. The method employs slow-
24 moving UAVs that acquire images along predefined trajectories near and around targeted trees, and
25 computer vision-based approaches that process the images to obtain detailed tree reconstructions.
26 After we confirmed the potential of the methodology via simulation we evaluated several UAV
27 platforms, strategies for image acquisition, and image processing algorithms. We present an original,
28 step-by-step workflow which utilizes open source programs and original software. We anticipate that
29 future development and applications of our method will improve our understanding of forest self-
30 organization emerging from the competition among trees, and will lead to a refined generation of
31 individual-tree-based forest models.

32 **1. Introduction**

33 Understanding how macroscopic patterns of forests emerge as a result of self-organization of individual
34 plants and how ecosystems respond to environmental gradients and disturbances that occur at different
35 spatial and temporal scales has long been reported as a largely unresolved fundamental ecological
36 challenge (Levin, 1998). The phenotypic plasticity of individual trees is regarded as the major biological
37 determinant of self-organization, structure, and dynamics of forested ecosystems and their response to
38 natural and anthropogenic disturbances (Strigul, et al., 2008; Strigul, 2012). Unique patterns of tree
39 plasticity have been identified across ecological and species groups, for instance, in conifers (Loehle,
40 1986; Umeki, 1995; Stoll & Schmid, 1998) and broad-leaf trees (Woods & Shanks, 1959; Brisson, 2001);
41 and biomes, including tropical (Young & Hubbell, 1991) and temperate ecosystems (Gysel, 1951; Frelich
42 & Martin, 1988; Webster & Lorimer, 2005). Failures to predict growth at the individual tree level with
43 acceptable accuracy have been attributed to the heterogeneity in geomorphic and climatic phenomena
44 affecting tree survival and growth, but primarily to inadequate information on the size, shape, and
45 spatial distribution of interacting trees (Strigul, 2012).

46 National Forest Inventory (NFI) systems are a major source of systematic, spatially distributed, and
47 repeated individual tree measurements obtained during field visits of established plots. A review of NFI
48 field protocols and data quality standards reveals that very precise measurements are prescribed for
49 tree stem diameter at breast height, and for fixed-area field plots, distances used in determining
50 whether a tree stem center is within the plot area. Where recorded, the relative position of tree stems
51 within a plot and tree height is measured accurately. Some vegetation parameters such as shrub and
52 forb percent cover, crown base height, and crown compaction ratio are assessed ocularly, and therefore
53 should be regarded more as estimates rather than measurements. Owing to cost, complexity, and
54 logistic constraints such as visibility, crown width and other specialized tree dimensionality
55 measurements are obtained only during special projects.

56
57 Information on individual trees over large areas is feasible only via processing of remotely sensed data.
58 High (submeter) resolution space- or airborne spectral imagery has been used to identify and delineate
59 individual tree crowns (Wulder et al., 2000; Leckie et al., 2005; Hirschmugl et al., 2007; Skurikhin et al.,
60 2013), and to assess parameters of crown morphology such as height, radius, and surface curvature
61 (Gong et al., 2002; Song, 2007) using various modeling approaches. Information extracted by manual
62 interpretation of aerial photographs has often been used as surrogate of field measurements for model
63 development and validation (Gong et al., 2002; Coulston et al., 2012). The advent of Light Detection and
64 Ranging (LiDAR) technology enabled 3D measurements of vegetation over forested landscapes.
65 Operated mainly from airborne platforms, LiDAR instruments emit short pulses of light that propagate
66 through the atmosphere as a beam of photons and are backscattered to the instrument from
67 illuminated targets. The loci of interactions with objects or object parts along a beam's trajectory are
68 determined with decimeter precision and reported as points georeferenced in three dimensions. The
69 collection of points generated across all pulses is referred to as a point cloud. A typical LiDAR data set of
70 a forested scene comprises points from the entire volume of tree crowns and ground surfaces. Models
71 operating on metrics that describe the spatial distribution of above-ground points have been proven
72 useful for assessing area-based forest inventory parameters such as wood volume and biomass (Zhao et
73 al., 2009; Sheridan et al., 2015). With high-density LiDAR data, a single mature tree can be represented
74 by many, up to hundreds of points, conditions conducive to a precise assessment of its dimensions,
75 including height and crown width (Popescu et al., 2003; Andersen et al., 2004). Often however, the
76 token representation of lower canopy components and ground surfaces in LiDAR data sets caused by
77 substantial attenuation of pulse energy in dense, multistory stands leads to less accurate estimates of
78 tree dimensionality (Gatziolis et al., 2010; Korpela et al., 2012). Terrestrial LiDAR systems operated from

79 ground or near-ground locations deliver point cloud densities orders of magnitude higher than those
80 generated by using airborne instruments, enabling detailed and precise reconstructions of individual
81 trees (Côté et al., 2009). Modeling of crown morphology supported by terrestrial LiDAR data has been
82 shown effective in assessing how trees grow in response to competition between and within crowns
83 (Metz et al., 2013). Point clouds generated from single scanning locations always contain gaps due to
84 partial target occlusion, either from parts of the targeted tree itself or from surrounding vegetation. As
85 occlusion rates, gap frequency, and gap size increase with canopy height, the error levels in tree
86 dimensionality estimates obtained by processing these point clouds also increase with height (Henning
87 & Radtke, 2006; Maas et al., 2008). Ensuring that estimate precision meets established standards
88 necessitates scanning targeted trees from multiple locations and then fusing the individual point clouds,
89 a complication that often is logically complex and costly.
90

91 To date, precise tree crown dimensionality and location data supportive of a rigorous modeling of
92 individual tree growth has been inhibited by feasibility, logistics, and cost. Measuring crown
93 characteristics by using established inventory methods is very time consuming and hardly affordable
94 outside special projects. Existing remote sensing methods of measuring tree crowns provide only partial
95 crown reconstructions. Airborne LiDAR data acquisitions require prolonged planning and are costly. As
96 an example, the minimum cost for a single airborne LiDAR acquisition with common specifications in the
97 US Pacific Northwest exceeds \$20,000 irrespectively of acquisition area size (Erdody & Moskal, 2010).
98 Transferring to and operation of terrestrial LiDAR instruments in remote forest locations and challenging
99 terrain is both labor intensive and time consuming. As a result, the assessment of tree growth and
100 competition relies on numerous simplifying, albeit often unjustified, assumptions such as of trees with
101 symmetric, vertical, perfectly geometric crowns growing on flat terrain, and illuminated by
102 omnidirectional sunlight. These assumptions propagate through modeling efforts and ultimately reduce
103 the validity of model predictions, thereby decreasing their utility (Munro, 1974; Strigul, 2012).
104

105 Recently, unmanned aerial vehicles (UAVs) equipped with inexpensive, off-the-shelf panchromatic
106 cameras have emerged as a flexible, economic alternative data source that supports the retrieval of tree
107 dimensionality and location information. Flying at low altitude above the trees and with the camera
108 oriented at a nadir view, UAVs acquire high-resolution images with a high degree of spatial overlap. In
109 such conditions, a point on the surface of a tree crown or a small object on exposed ground is visible
110 from many positions along the UAV trajectory and is depicted in multiple images. Automated
111 photogrammetric systems based on computer Vision Structure from Motion (VSfM) algorithms (Snavely
112 et al., 2008) explore this redundancy to retrieve the camera location the moment an image was
113 acquired, calculate an orthographic rendition of each original image, and ultimately produce a precise
114 3D point cloud that represents objects (Dandois & Ellis, 2010; Rosnell & Honkavaara, 2012). Application
115 of VSfM techniques on UAV imagery has enabled accurate 3D modeling of manmade structures, bare
116 ground features, and forest canopies (de Matías et al., 2009; Danbois & Ellis, 2013; Dey et al., 2012).
117 Automated image processing is now supported by open-source and commercial software packages.

118 Image acquisitions with nadir-oriented cameras onboard UAVs, however, face the same issues as
119 airborne imagery; the great majority of points in derived clouds are positioned near or at the very top of
120 tree crowns. The representation of crown sides tends to be sparse and contains sizeable gaps, especially
121 lower in the crown, a potentially serious limitation in efforts to quantify lateral crown competition for
122 space and resources, as in the periphery of canopy openings. In this study, we extend UAV-based image
123 acquisition configurations to include oblique and horizontal camera views and UAV trajectories around
124 trees or tree groups at variable above-ground heights to achieve comprehensive, gap-free
125 representations of trees. To overcome the challenges imposed by these alternative UAV/camera

126 configurations, we evaluated many UAV platforms and open-source VSfM software options, and
127 developed original, supplementary programs. To determine whether comprehensive tree
128 representations are attainable, we initially processed synthetic imagery obtained via simulation. We
129 finally evaluated the efficacy and performance of our workflow targeting trees of different species,
130 shapes, sizes, and structural complexity.
131

132 **2. Method development and testing**

133

134 *2.1. Image processing*

135

136 The procedure that uses a set of images exhibiting substantial spatial overlap to obtain a point cloud
137 representing the objects present in the images contains three main steps: feature detection, bundle
138 adjustment, and dense reconstruction. To implement this procedure, we have carefully examined a
139 variety of software available for image processing. The workflow presented below was found by
140 experimentation to be the most efficient for our project. We employed a sequence of computer
141 programs, most of which are available as freeware or provide free licenses to academic institutions. The
142 software used includes OpenCV libraries, VisualSfM, CMVS, SURE, OpenGL, and Mission Planner, with
143 each of them accompanied by a comprehensive manual. Considering that the majority of the software
144 listed above evolves rapidly, we intentionally refrained from duplicating here elements of associated
145 manuals to which we refer a reader in addition to our presentation.
146

147

148 Feature detection is based on the identification of image regions, often called keypoints, pertaining to
149 structural scene elements. Thanks to image overlap, these elements are present in multiple images, but
150 because their position relative to the focal point of the camera is image-specific, they are depicted in
151 different scale and orientation (Figure 1). Illumination differences and image resolution can impose
152 additional feature distortions. Algorithms used in feature detection explore principles of the scale-space
153 theory (Lindeberg, 1998). According to this theory, a high-resolution image can be perceived as a
154 collection of scene representations, called octaves, in Gaussian scale space. The scale space can be
155 obtained by progressively smoothing the high-resolution image, an operation analogous to a gradual
156 reduction of its resolution. If robust against changes in scale and orientation, the characteristics of a
157 keypoint identified on a given octave of one image can be used to identify the same keypoint on other
158 images. The algorithms proposed for feature detection in this context include the Scale Invariant Feature
159 Transform (SIFT) (Lowe, 2004), the Speeded Up Robust Features (SURF) (Bay et al., 2008), and the
160 Oriented FAST and Rotated BRIEF (ORB) (Rublee et al., 2011). We employed SIFT in our workflow as it is
161 currently the reference approach in the field of computer vision. To identify keypoints, SIFT initially
162 applies to each image octave an approximation of the Laplacian of Gaussian filter known as Difference of
163 Gaussians, an efficient edge detector. Identified SIFT keypoints are circular image regions, each
164 described by a set of parameters: the image coordinates at the center of the region, the radius of the
165 region and an angle. The radius and angle of each keypoint serve as scale and orientation indicators
166 respectively (Figure 1). Keypoints are further characterized by a descriptor of their neighborhood,
167 determined from the values of pixels in the vicinity of the keypoint's center and usually encoded into a
168 vector of 128 values. By searching for keypoints at multiple scales and positions, SIFT is invariant to
169 image translation, rotation, and rescaling, and partially invariant to affine distortion and illumination
170 changes. It can robustly identify scene features even in images containing substantial amounts of noise
or under partial occlusion.
171

172

Figure 1 (about here). SIFT-based scene keypoint detection and matching on two overlapping images.

173 *Top: Original images; Middle: 1464 (left) and 1477 (right) keypoints with arrows denoting orientation
174 and radii scale; Bottom: 157 keypoint pairs, matched by color and number.*

175
176 The bundle adjustment process initially compares keypoint descriptors identified across images to
177 determine two similar images. Then, an optimization procedure is performed to infer the positions of
178 cameras for these two images. Remaining images are added one at a time with relative positions further
179 adjusted, until camera locations become available for all images. The optimization often uses the
180 Levenberg-Marquardt algorithm (Levenberg, 1944; Marquardt, 1963), a general purpose non-linear
181 optimization procedure. Heuristics and prior information, such as GPS coordinates of UAV locations at
182 the moment an image is acquired, can be included to improve convergence speed. In the end, the
183 spatial positions and orientations of all cameras are triangulated using the keypoints identified in the
184 previous step. At the conclusion of bundle adjustment a so-called sparse 3D model that contains the 3D
185 positions of all identified features becomes available. We implemented the feature detection and
186 bundle adjustment components of our workflow in VSFM software (Wu, 2013; Wu et al, 2013).
187

188 In dense reconstruction, the final processing step, all image pixels, not only keypoints, along with the
189 positions and orientations of each camera, are merged into a single high-density structure. This is
190 achieved by matching pixels with similar value across pictures with respect to the epipolar geometry
191 constraints (Zhang et al., 1995) of the sparse model. The epipolar geometry is defined for each image
192 pair. It includes a baseline connecting the locations of the two cameras that are known from the sparse
193 model, the oriented image planes, the image locations where image plane and baseline intersect known
194 as epipoles, and the epipolar lines connecting a camera location with a pixel on the image plane. By
195 restricting searches for a pixel match along the epipolar lines, processing is greatly expedited. In our
196 workflow, we considered CMVS (Furukawa & Ponce, 2010) and SURE (Rothermel et al., 2012), two state-
197 of-the-art, freely available multi-core implementations, which adopt different strategies to generating
198 the dense model. CMVS is a patch-based method which starts from matched keypoints and generates
199 local models of object surfaces, or patches, in the immediate neighborhood of the keypoints. These
200 patches are then expanded until their projections on the original pictures eventually form a dense tiling.
201 SURE's approach is based on the computation of depth maps for a set of reference images, based on the
202 disparity between these images and other images obtained from nearby, according to the sparse model,
203 positions. Each depth map provides a dense model of pixels equivalent to a local reconstruction from
204 one reference viewpoint. All partial reconstructions are eventually merged to obtain a dense
205 reconstruction for the entire scene.
206

207 The sparse and dense reconstructions obtained from a set of overlapping images are configured in the
208 same internal coordinate system and scale. Conversion to real-world orientation and coordinate system
209 is a prerequisite for meaningful measurements of reconstructed objects or for comparisons with
210 ancillary spatial data. Such conversions can be performed manually on the reconstructed scene,
211 assuming reference *in-situ* measurements of object dimensionality are available. In this study, we used
212 an alternative, automated approach. The latitude, longitude, and elevation of camera locations recorded
213 by a recreational-grade GPS device onboard the UAV were converted to orthographic Universal
214 Transverse Mercator (UTM) coordinates using a GDAL (2015) reprojection function. The rotation/
215 translation matrix linking the UTM and sparse model coordinates of the camera positions was then
216 calculated via maximum likelihood, and applied to convert the sparse model coordinates system to
217 UTM. All subsequent processing by CMVS and SURE were performed on the UTM version of the sparse
218 model.
219

220 *2.1.1 Image calibration*

221
222 All imaging systems introduce a variety of distortions onto acquired imagery. The magnitude of the
223 distortion is usually negligible in professional systems, but it can be substantial for inexpensive, off-the-
224 shelf cameras used in structure from motion applications (Balletti et al., 2014). Most software, including
225 VSfM, perform internal image calibration using information on the focal length of the lens, usually
226 stored in the header of the image, and a generic rectification process, or undistortion as it is commonly
227 called. Departures between the actual distortion and the one anticipated by the generic rectification
228 process reduce the spatial accuracy of reconstructed objects. Using simulated and UAV-based, nadir
229 looking imagery featuring sparse and low vegetation on flat land, Wu (2014), the author of the VSfM
230 software, documented that scene reconstructions obtained by using the generic image calibration
231 model present in VSfM produced a macroscopically concave ground surface, an artifact attributed to
232 imprecise image calibration. To avoid artifacts, we first calibrated all cameras used in this study with the
233 efficient procedure described in the OpenCV image processing library (Bradski, 2000), and then
234 instructed VSfM to skip the generic image calibration process. Separate calibrations were performed for
235 each operating mode of each camera. As expected, and evident in Figure 2, calibration effects were
236 more discernible near the periphery of the image. The convex scene horizon in the original image
237 appears flat and horizontal after calibration and the local road pavement on the lower left part of the
238 original image is excluded from the calibrated version.
239

240 ***Figure 2 (about here). Removal of lens distortion.***

241 Demonstration of a. original, vs. b. OpenCV-calibrated lateral tree image obtained with a UAV-based
242 GoPro camera at an above-ground altitude of 18 meters. Horizontal red line drawn to illustrate form of
243 horizon in each version of the image.

244
245 *2.2. Simulation-based assessment of image-based tree reconstruction accuracy*

246 Upon initial consideration, the accurate and detailed reconstruction of objects characterized by complex
247 structure and geometry, such as trees, using image-based techniques may be deemed an ill-fated effort.
248 The main reason for pessimistic prognoses is that the aforementioned methods and algorithms used in
249 processing the imagery anticipate planar surfaces as structural elements of the objects and well-defined
250 edges at object surface intersections. Except for the lower part of the main stem of large trees, sizeable
251 and homogeneous surfaces separated by crisp boundaries are absent in trees. A second reason is that
252 trees are not opaque objects. Even in high foliage and branch density conditions, portions of scene
253 background are clearly visible through the tree crowns. The see-through-crown phenomenon can be
254 overlooked in nadir-oriented imagery where the forest floor is acting as tree background, but it is often
255 rather pronounced in lateral imagery where the depth of the part of the scene situated behind the trees
256 can be large. The term ‘lateral’ is used here to describe images acquired with the UAV positioned to the
257 side of the tree and lower than the tree top. The effects of substantial differences in parallax between
258 tree components and background depicted only pixels apart in lateral tree imagery, and high rates of
259 component occlusion, are likely analogous to image distortion, a condition to which the SIFT algorithm is
260 only partially invariant. Furthermore, the upper parts of tree crowns depicted in lateral imagery can
261 have the sky as background instead of the typically darker vegetation or terrain background present in
262 nadir-oriented imagery. Drastic changes in background brightness, for instance, from sky to vegetation
263 and back to sky, behind a given part of a tree crown that appears across multiple overlapping lateral
264 images, influence the red, green, and blue (RGB) values of image pixels corresponding to that crown
265 part. The ensuing variability in pixel values often mimics effects induced by differences in diurnal solar
266 illumination regimes. Illumination variability is another condition to which SIFT is only partially invariant.
267

269 We used simulation and synthetic images to evaluate the robustness of our standard workflow to the
270 idiosyncrasies of lateral tree imagery described above. We relied on terrestrial LiDAR data representing
271 a collection of free-standing trees, each scanned from multiple near-ground locations. The scanning was
272 performed in high-density mode with the laser beams distributed in fine horizontal and vertical angular
273 increments (0.4 mrad). Each point in the generated clouds was furnished with RGB values extracted
274 from panchromatic imagery captured by the LiDAR instrument during the scanning. Details on the data
275 acquisition are available in Gatziolis et al. (2010). The RGB-colored point cloud of each tree was then
276 visualized in an OpenGL interface (Shreiner, 2009) with perspective rendering (Figure 3a). In this virtual
277 visualization environment, RGB-colored snapshots of each scene, henceforth referred to as synthetic
278 images, can be obtained without limitations on image number, resolution, amount of spatial overlap,
279 and format type. By specifying the trajectory, orientation, snapshot frequency, and field of view of the
280 virtual camera and also the pixel dimensionality of the OpenGL interface, we can control the scale at
281 which targeted trees, or parts of trees, are represented in the synthetic imagery. The background can be
282 adjusted to resemble the overall scene illumination conditions effective during the acquisition of the
283 terrestrial imagery, including illumination adjustments along azimuth and sun elevation angle gradients.
284 Synthetic images generated by exercising combinations of these options yield very realistic
285 approximations of imagery obtained onboard the UAVs, with the additional advantage that the
286 dimensionality of the objects depicted in the imagery is precisely known. Point clouds generated by
287 processing the synthetic imagery can then be compared to the original terrestrial LiDAR point cloud to
288 evaluate the accuracy and precision of object reconstructions.
289

290 **Figure 3 (about here). 3D reconstruction in simulation.**

291 *a. Perspective view of point cloud acquired with terrestrial LiDAR and camera locations (red spheres)*
292 *used to obtain virtual images of the scene. b. Scene reconstruction obtained by processing of the images.*

293
294 For our simulations we employed a 2500 by 2000 pixel (5 Mp) virtual camera. The camera was
295 positioned on a circular trajectory centered on the crown of each of the trees depicted in the terrestrial
296 LiDAR point clouds. The camera trajectory was either aligned to a horizontal plane elevated to
297 approximately the vertical middle of the crown, or along a spiral ascent from the 15th to the 85th
298 percentile of tree height (Figure 3a). Camera distance to the nearest part of a crown was between 10
299 and 15m and scene background was set to black. Between 100 and 250 synthetic images were acquired
300 for each tree and trajectory combination, initially in BMP (bitmap) format and subsequently converted
301 to the Joint Photographic Experts Group (JPEG) format, required by VSFM, using a maximum quality
302 setting in ImageMagick, an open-source software suite (<http://www.imagemagick.org>). The synthetic
303 imagery for each tree was processed with VSFM using standard settings, and the coordinates of the
304 resulting point clouds generated at the sparse reconstruction stage were converted to the coordinate
305 system of the terrestrial LiDAR data using the locations of the virtual camera known from the simulation
306 settings. Dense reconstructions were obtained by using SURE with standard setting plus an option to
307 ignore synthetic image regions with very low variability in pixel values, as those representing the scene
308 background.
309

310 The original Terrestrial LiDAR and dense reconstruction point clouds for each tree were compared in
311 voxel space (Popescu & Zhao, 2008; Gatziolis, 2012). In this setting, the bounding box of a point cloud is
312 exhaustively partitioned into discrete, equally-sized cubical elements, called voxels. Those voxels
313 containing one or more points are labeled ‘filled’, all others remain empty. By ensuring that the
314 terrestrial and reconstruction voxel spaces have the same origin and voxel size, we were able to
315 calculate the spatial correspondence of filled voxels between the two clouds and the rates of omission
316 and commission, and identify parts of the voxel space where correspondence is better or worse than in

317 other parts. The size, or resolution, of the voxels was set to 2cm, in response to the angular resolution
318 of the terrestrial LiDAR beams at the mean distance between trees and LiDAR instrument.

319
320 *2.3. UAV platform characteristics and image acquisition procedures*
321

322 After a preliminary evaluation of several commercially available UAV platforms, we focused on an
323 APM:Copter (<http://copter.ardupilot.com>), a hexacopter rotorcraft (Figure 4), because of its easily
324 modifiable architecture and open source software for flight control. We also used a commercial IRIS
325 quadcopter developed by 3DRobotics (<http://3drobotics.com>). The components of the customized
326 hexacopter and their purchasing prices are shown in Table 1. Both systems feature gyroscopes and GPS
327 receivers. Compared to systems available in the market, our hexacopter is an inexpensive but versatile
328 configuration whose component acquisition cost is expected to drop substantially in the future as UAV
329 technology evolves and its popularity continues to increase.
330

331 Table 1. Specifications and prices of customized UAV platform used in this study at the time of writing.

Component description	March 2015 price (\$)
DIJ F550 Hexacopter Frame with 6 motor controllers and brushless motors	200
3D Robotics Pixhawk flight controller	200
Microprocessor: 32-bit STM32F427 Cortex M4 core with FPU, 168 MHz/256 KB RAM/2 MB Flash, 32 bit STM32F103 failsafe co-processor	
Sensors: ST Micro L3GD20 3-axis 16-bit gyroscope, ST Micro LSM303D 3-axis 14-bit accelerometer / magnetometer, Invensense MPU 6000 3-axis accelerometer/gyroscope, MEAS MS5611 barometer	
3D Robotics GPS with compass	90
915 Mhz telemetry radio and transmitter to controller	30
FrSky receiver	30
Spectrum DX7 transmitter	200
Tarot T-2D brushless camera gimbal	150
GOPRO 3+ Black Edition sport camera	350
LIPO batteries	60

332
333
334 **Figure 4 (about here). Custom built UAV hexacopter used to collect imagery data in this study.**
335
336 Both UAVs used in this study can be operated either autonomously along a predefined trajectory or
337 manually. The manual flight control requires expertise and continuous line of sight between the system
338 and the operator. Maintaining nearly constant planar and vertical speed and orientation of the onboard
339 camera towards the target is challenging, even for operators with years of experience. Experimentation
340 confirmed that imagery acquired with manual flight control exhibits variable rates of overlap between
341 frames captured sequentially. Smaller components of the targets are sometimes depicted in too few
342 frames or are missing completely, while others appear in an excessive number of frames. For these
343 reasons, it was decided to rely on autonomous flights configured by prior mission planning, and reserve
344 the manual mode only for intervention in the event of an emergency.
345

346 *2.3.1. Characteristics of the imaging system*
347

348 We conducted extended trials with several cameras, including the sport GOPRO 3+ Black Edition
349 (<http://gopro.com/>), Ilook Walkera (<http://www.walkera.com/en/>) and Canon PowerShot
350 (<http://www.canon.com>). The evaluations involved all operating modes offered by each camera,
351 including normal, wide, and superwide zoom settings, as well as acquiring video and then extracting
352 individual frames with post-processing. At the conclusion of the trials, we selected the GOPRO 3+ Black
353 Edition operated in photography mode, and normal, 5 Mp resolution. Acquired frames were stored in
354 JPEG format to the camera's flash card. We rarely achieved event partial tree reconstruction using the
355 alternative settings, likely because of the magnitude of distortion embedded into the imagery.
356

357 *2.3.2. Mission planning*

358

359 The objective of the mission planning phase is to optimize the UAV trajectory, attitude, speed, and were
360 applicable, the view angle of the camera gimbal for image acquisition. The gimbal is a hardware
361 component which allows the orientation of the camera to be modified during the flight relative to the
362 platform. Dynamic, trajectory-location-specific adjustments of camera orientation can be used to ensure
363 that the target is centered on the images, especially when the UAV trajectory is not along a horizontal
364 plane. During mission planning the image acquisition frequency is also considered. After rigorous
365 evaluation of various UAV trajectory templates (Figure 5), we determined that the optimal
366 reconstructions of trees are achieved when sequential images have a field-of-view overlap of
367 approximately 70%. In this configuration, the nominal mean number of images where a part of a
368 targeted tree would be present in is 3.4. Once determined, a trajectory template is centered on the
369 target and scaled so that during the actual flight the mean camera-tree distance, platform speed, and
370 image acquisition frequency will generate images exhibiting the targeted field-of-view overlap. The
371 process is perceptually simple, but technically complex considering that all directional and attitudinal
372 vectors of the UAV have to be converted to instructions passed to the UAV controller. Thankfully, it can
373 be streamlined by using Mission Planner, an open-source software suite developed by Michael Osborne
374 (<http://planner.ardupilot.com>). Mission Planner relies on user input and georeferenced imagery of the
375 targeted area and tree(s), to establish the geographic (latitude and longitude) coordinates of the UAV's
376 starting and ending position and trajectory. A small set of high-level Mission Planner commands can
377 accomplish even complex trajectory templates. All templates shown in Figure 5 require only 5
378 commands (Table 2). Our typical setup uses a location positioned in the middle of an open area for both
379 the start and end of the flight. The UAV would initially ascend vertically above its starting location to a
380 pre-specified height, then move horizontally to the beginning of the trajectory, complete it, and finally
381 return to the starting location. In the present development state of our system, it is the user's
382 responsibility to ensure that the designed flight path is free of other objects, an easy to achieve
383 requirement considering the wealth of georeferenced, high resolution, publicly available aerial
384 photographs (Figure 6). The Mission Planer is also used to convert telemetry data of camera locations
385 the moment images were acquired, provided by the GPS receiver stored to the onboard flash memory
386 card, to an accessible format. As detailed in Section 2.1, these locations are later paired to those
387 calculated during the sparse reconstruction processing phase to adjust the scale and georeference of
388 reconstructed objects.
389

390 Table 2. Mission Planner commands used for autonomous UAV flights

Command	Code	Description
WAYPOINT	16	Latitude, longitude (in degrees) and altitude vector (in meters) of locations visited during a flight

DO_CHANGE_SPEED	178	Speed, in meters per second. Calculated considering distance to target and image acquisition frequency, usually 2Hz. Typical speed value is 4 meters per second
DO_SET_ROI	201	Vector of UAV heading planar azimuth and gimbal angle (in degrees) that orients the camera towards relative to a specified point of interest.
RETURN_TO_LAUNCH	20	Return to launch location after flight completion
DO_SET_HOME	179	Latitude and longitude vector (in degrees) of return UAV location to use in the event of an emergency, or system anomaly

391

392

393 **Figure 5 (about here). Different UAV trajectories tested for image acquisition.**

394 *a. circular, at constant height; b. ‘stacked circles’, each at different above-ground height, for tall trees*
395 *(height more than 20 m); c. spiral, for trees with complex geometry; d. vertical meandering, targeting*
396 *tree sectors; e. clover, for trees with wide, ellipsoidal tree crowns; f. ‘spring-hemisphere’, designed for*
397 *trees with flat-top, asymmetrical crowns; g. ‘nested circles’, centered on the tree; and h. ‘jagged saucer’,*
398 *designed for trees with dense foliage but low crown compaction ratio.*

399

400 **Figure 6 (about here). Visualization of designed and accomplished UAV trajectories.**

401 *a. and c. circular and clover templates as seen in Mission Planner with yellow lines showing the flight*
402 *paths, green balloons indicating waypoints, and red balloons the center of targeted trees. b. and d.*
403 *perspective scene view in Google Earth, with yellow pins indicating camera locations along each*
404 *trajectory at the moment images were captured.*

405

406 **2.4 Evaluation of tree reconstructions**

407

408 Processing of the synthetic imagery always produced complete tree reconstructions. The number of
409 points in the reconstruction ranged between 20 and 25 percent of those present in the original
410 terrestrial LiDAR point cloud (Figure 3b). Larger percentages could be achieved by increasing the
411 resolution of the virtual camera, at the expense of prolonged processing time in both VSfM and SURE.
412 Volumetric comparisons in voxel space revealed excellent agreement between LiDAR and reconstructed
413 point clouds, with a mean of 94 percent of filled voxels collocated. Omnidirectional jittering of the voxel-
414 rendered tree reconstructions relative to the terrestrial LiDAR equivalent always resulted in a
415 substantial, 30 to 40 percent reduction in collocation rates, even when the jittering was limited to a
416 single voxel. The rapid reduction in the collocation rates caused by jittering limited to one voxel suggests
417 that the scaling and translation of the derived point cloud relative to the original terrestrial LiDAR cloud
418 is accurate and precise. It also implies that the coordinates of the virtual camera positions deduced by
419 VSfM during the processing of the synthetic imagery and those used in the simulation are identical up to
420 the scale difference. Once calculated, scaling and translation of the reconstructed point cloud
421 performed by using this relationship rendered the derived tree point cloud a thinned copy of the original
422 terrestrial point cloud. Our simulation results suggest that the absence of planar surfaces and lack of
423 opacity in tree crowns do not impose systemic restrictions to the surface-from-motion approach we
424 used to obtain the 3D tree representations.

425

426 By exploring several virtual camera trajectory patterns while altering the image acquisition frequency in
427 each of them, we were able to quantify the effects that different patterns and image field-of-view
428 overlap percentages have on tree reconstruction accuracy (Figure 7). Even in the ideal, noise-free

429 environment of the simulations, a minimum 30 percent image overlap was required for complete target
430 reconstructions. For patterns involving camera locations at variable above-ground heights the minimum
431 percentage was higher, between 35 and 40 percent. Below a mean 45 percent overlap, all simulations
432 were susceptible to failure, pending on the image pair selected for initiating the matching process
433 described in section 2.1. For the circular trajectory pattern, the level of volumetric correspondence
434 between the terrestrial LiDAR and imagery-derived point clouds would increase rapidly at low field-of-
435 view overlap percentages and then progressively decline until reaching an asymptote, usually at 90
436 percent volumetric correspondence or higher (Figure 7). Complete reconstructions obtained with the
437 spiral trajectory usually required at least 35 percent image overlap. The observed volumetric
438 correspondence to the LiDAR point cloud showed a sigmoidal increase with higher image overlap
439 percentages until reaching an asymptote level, sometimes as high as 94 percent.
440

441 *Figure 7 (about here). Accuracy and completeness of reconstruction for a Pinus ponderosa tree.*

442 *This analysis is based on synthetic imagery simulated using visualization of terrestrial LiDAR point clouds*
443 *and two camera trajectories. Percentage of collocated filled voxels is used as reconstruction*
444 *completeness criterion.*

445 In a spiral acquisition trajectory yielding the same number of images of a targeted tree as a circular
446 trajectory, the horizontal overlap percentage between two sequential images is lower. Unlike the
447 circular trajectory, though, in the spiral there is vertical overlap with images obtained after the UAV has
448 completed a rotation around the tree. While the overall mean overlap between the two trajectory
449 patterns was the same in our simulations, the spiral had lower overlap percentage between any two
450 images selected for the initiation of the matching process, and therefore more likely to fail to yield a
451 complete reconstruction when the overall overlap image rate was low. Owing to the vertical image
452 overlap present in spiral UAV missions, selected parts of the tree are visible from more than one vertical
453 viewing angles, an arrangement that reduces target occlusion rates. For tree species with dense,
454 uniform distribution of foliage and deeply shaded crown centers, the variability in vertical view angles
455 offered by the spiral trajectory pattern may be unimportant. For species with predominantly horizontal
456 or angular branch arrangement and lower crown compaction rates, vertical viewing variability allows
457 internal crown components to be represented adequately in the derived point cloud. Three out of four
458 of the voxels accounting for the approximately 4 percent difference in reconstruction completeness
459 between the spiral and circular UAV trajectories around a Red Pine (*Pinus ponderosa*) tree at 70 percent
460 image overlap rates or higher (Figure 7) were located in the internal half of the crown.
461

462 Most UAV flights also produced complete tree reconstructions (Figures 8 and 9). In the absence of
463 detailed crown dimensionality measurements, we relied on ocular assessment of reconstruction
464 accuracy and precision. The typical example shown on Figure 8, obtained with the spiral UAV trajectory
465 (Figure 5c), among our most reliable for complete target reconstruction, shows that even the shaded
466 components of the tree crown interior are represented. Many parts on the upper quarter of the crown
467 have a light blue hue inherited from the sky background in corresponding UAV images. Although less
468 evident, selected parts of the lower crown exhibit similar ground-influenced coloring. The coloring
469 artifacts shown in Figure 8 appear where the image area occupied by an identified keypoint is
470 dominated by a uniformly colored background. Sometimes these anomalies are limited to the RGB
471 values assigned to points and can be overlooked if the main objective of the UAV mission is the retrieval
472 of tree dimensionality. Often though they represent an overestimation of tree crown volume and must
473 be removed (Figure 10). Accomplishing this task with manual intervention is laborious and subjective.
474 The task can be easily automated for points pertaining to a sky background thanks to their markedly
475 different RGB values compared to those of vegetation. Where suitable RGB value thresholds cannot be
476

477 safely identified, as it is usually the case for the lower parts of trees, we found it useful to trim the depth
478 of the part of the overall reconstructions that is derived from each image, so that only the portion
479 nearer the camera position is retained. SURE facilitates this procedure by providing a separate dense
480 reconstruction for each processed image organized in a common coordinate system. The complete
481 reconstruction can be obtained by merging the trimmed parts. In the absence of precise reference data,
482 we were unable to determine quantitatively the significance of these artifacts.
483

484 **Figure 8 (about here). Orthographic horizontal view of reconstructed point cloud and UAV-based**
485 **oblique perspective image.** Colored arrows denote corresponding tree crown components.
486

487 **Figure 9 (about here). Illustration of comprehensive tree reconstructions (right column) and reference**
488 **UAV-based images (left column).**
489

490 **Figure 10 (about here). Demonstration of artifacts in the 3D tree reconstruction pertaining to a single**
491 **UAV image.** a. Initial reconstruction, positioned facing the camera with a band of white-colored points
492 belonging to sky background near the top, and light colored points to the sides belonging to fallow land
493 background, b. Side view, with camera position to the left and sky points in oval and land points in
494 rectangle, and c. Trimmed reconstruction positioned facing the camera.
495

496 The ‘nested circle’ and ‘jagged saucer’ trajectories (Figure 5g and 5h) produced only partial
497 reconstructions and several disjointed models in VSfM and are, therefore, not recommended, while the
498 altitude variability in the ‘meandering’ trajectory (Figure 5d) was often responsible for premature
499 mission termination owing to rapid depletion of the UAV batteries. Partial reconstructions were the
500 norm, rather than the exception, when for a portion of the mission the camera was positioned directly
501 against the sun. In such conditions the shaded portion of the crown would either not be reconstructed
502 at all, or it would be organized in separate 3D models with much lower point density and sizable gaps. In
503 the example shown in Figure 11, the GPS recorded and process-derived positions of the camera on
504 board the UAV show a nearly perfect correspondence for three quarters of the circular UAV trajectory.
505 GPS recordings are half as many as the camera positions because of limitations in the recording
506 frequency of the GPS device. It should be noted that pending on the hardware configuration of the UAV
507 and the number of peripheral devices connected to it, it is sometimes necessary to operate below the
508 capacity of a particular device to either conserve energy, or to avoid overwhelming the UAV controller.
509 Based on our experience, a close fit between recorded and derived camera positions practically
510 guarantees that a complete target representation will be obtained during the dense reconstruction
511 phase. The remaining part of the trajectory, where the camera is positioned against the sun, was
512 actually derived from a separate model and shows a poor fit, resembling more of a linear transect than a
513 circular arc. As the camera moves from partially to completely against the sun, image contrast is
514 reduced, and the radii of identified keypoints become smaller. Radius reductions increase the
515 uncertainty associated with keypoints orientation and descriptor. We suspect that changes in the
516 magnitude of the mean image keypoint radius are manifested as variability in the distance between the
517 tree and calculated camera locations, evident in the misfit part of the VSfM-derived camera trajectory
518 shown in Figure 11.
519

520 **Figure 11 (about here). Comparison between real and reconstructed trajectory.** Nadir view of
521 reconstructed tree with camera GPS locations at image frame acquisition moments (yellow circles) and
522 VSfM-calculated locations (red dots). Frame frequency 2Hz, GPS fixes at 1Hz. Inset at the lower left
523 shows lateral view of the reconstructed tree.
524

525 On a few occasions, we observed more than one, nearly parallel, and closely stacked layers of points
526 representing the ground, likely an artifact of texture uniformity in those parts of the scene. The use of
527 calibrated imagery has expedited the computations for identifying camera positions and for generating
528 the sparse reconstructions in VSfM and has reduced the rate of partial reconstruction occurrence.
529 However, its effect on the accuracy of the reconstruction obtained using SURE was unclear.
530

531 **3. Discussion**

532 Our results indicate that a meticulously planned image acquisition mission, namely a judicious selection
533 of flight trajectory, UAV speed, and image acquisition frequency, will deliver a comprehensive dense
534 reconstruction of targeted vegetation, except perhaps in unfavorable sun illumination and wind
535 conditions. As explained in section 2.1, our workflow relies on keypoints, most of which are identified
536 along image discontinuities. A smooth flight trajectory around the target ensures that sequential images
537 contain an adequate number of similar keypoints from which the camera location effective for each
538 image capture can be calculated with adequate precision. Where the smooth change in the field of view
539 between two sequential images is interrupted, the offending image becomes the first in a separate
540 model. Bundle adjustments can reduce the frequency of separate model emergence but they cannot
541 eliminate it. The often advocated practice of adding to a model image frames originally put by VSfM to a
542 separate model without performing bundle adjustment after each frame addition may be warranted for
543 manmade objects but is not recommended for trees because it leads to obvious reconstruction artifacts.
544 Mission plans for flights expected to occur during bright solar illumination conditions using gimbal-
545 equipped UAVs could be adjusted to avoid camera positioning directly against the sun. This can be
546 accomplished by specifying a slightly downward, oblique camera orientation. The precise solar elevation
547 angle and azimuth for any location can be obtained from the NOAA Solar Position Calculator
548 (<http://www.esrl.noaa.gov/gmd/grad/solcalc/azel.html>), or can be computed as described in Reda &
549 Andreas (2008).
550

551 GPS-equipped UAV platforms not only enable preprogrammed navigation, but also, and perhaps equally
552 importantly, can be used for a precise scaling of reconstructed tree point clouds to actual dimensions.
553 The GPS receivers placed on the two UAVs employed in this study offer recreational grade precision, and
554 as such, their individual position recordings may contain an absolute error of a few meters. In our trials,
555 however, the relative error between trajectory recordings appeared to always be less than a meter, in
556 most cases about half a meter. This is based on the observation that our UAVs, initially placed on a
557 launch pad measuring about 60 cm on each side, would return at the completion of the mission with
558 their landing gear partially on the launch pad. Fitting the VSfM-calculated camera locations to
559 corresponding GPS recordings containing a relative positional error of such magnitude, would yield point
560 cloud scaling errors of 0.5 percent or lower, a level deemed adequate for UAV imagery and structure
561 from motion based assessment of yearly tree growth. In the absence of GPS recordings, the scaling of
562 the point cloud would have to be performed manually using georeferenced imagery.
563

564 Except for extremes in solar illumination conditions such as sun facing camera exposures or at dusk,
565 disparities in light distribution may actually be beneficial for structure-from-motion-based applications
566 in natural environments because they accentuate feature edges. As it is evident in the tree portion
567 between the red and purple colored arrows shown in Figure 8, crown parts in the penumbra are still
568 represented, albeit with reduced point density. Image enhancements focusing on shaded or very bright
569 parts could perhaps be used to ameliorate the direct sunlight effects or improve the reconstruction
570 density for shaded areas.
571

572

573 To account for absolute GPS receiver and ancillary imagery registration errors, current UAV missions
574 must be planned with adequate clearance from any scene objects. We were able to comply with this
575 requirement in our trials because we mostly targeted individual trees or small groups of trees growing in
576 open space. Extending our operations to confined areas, for instance descending into and proceeding
577 near and along the periphery of forest openings, would require much higher navigation precision.
578 Thankfully, obstacle avoidance has been actively researched and several solutions specific to forested
579 environments have been proposed (Frew et al., 2006; Karaman and Frazzoli, 2012; Mori and Scherer,
580 2013; Roberts et al., 2012; Ross et al., 2013). In particular, Ross et al. (2013) demonstrated full flight
581 control in forested environments using an UAV platform similar to ours. They used a low-resolution
582 camera mounted on a quadcopter that was outsourcing via a wireless connection all computationally
583 intensive image processing to a ground station, a standard laptop computer. Using this setup, they were
584 able to achieve a constant speed of 1.5 meters per second while avoiding trees. The rapidly expanding
585 onboard processing capabilities of UAVs suggest the possibility, in the near future, of coupling the 3D
586 reconstruction methodology proposed here with autonomous flight, thereby eliminating the need for
587 meticulous mission planning.

588
589 It is often tempting to acquire images with the highest possible frequency and maximum overlap. Action
590 cameras similar to those used in this study support high frame rates and carry ample image storage
591 space without affecting the payload and thus compromising the UAV's flight duration or mission
592 flexibility anyway. Large number of images though requires prolonged processing. Our simulations
593 indicate that image field-of-view overlap higher than 70 percent, does not improve the accuracy or
594 completeness of tree reconstructions. Visual assessments suggest that this is also true for actual UAV
595 imagery. Mission planning designed so that target features are represented in three to four images likely
596 maximizes the information content present in an acquisition and it is therefore recommended as an
597 initial mission configuration.

598
599 **4. Conclusion**
600
601 Rapid developments in UAV technology and enhancements in structure from motion software have
602 enabled detailed representation of manmade objects. In this paper, we describe how this technology
603 can inexpensively be extended to representations of natural objects, such as trees or groups of trees.
604 After extensive experimentation that involved several UAV platforms, cameras, mission planning
605 alternatives, processing software, and numerous procedural modifications and adjustments, our
606 workflow has been proven capable of handling most conditions encountered in practice to deliver
607 detailed reconstruction of trees. In addition to robust performance, our imaging system can be
608 employed rapidly in support of time-sensitive monitoring operations as, for instance, the assessment of
609 forest fire damage or progress of forest recovery from disturbance. It is also well suited to providing tree
610 dimensionality data through time, a prerequisite for improved models of tree growth and for an
611 accurate assessment of tree competition and morphological plasticity.

References Cited

1. Andersen, H.-E., Reutebuch, S.E., & McGaughey, R.J. (2006) A rigorous assessment of tree height measurements obtained using airborne lidar and conventional field methods. *Can J Rem Sens* 32(5): 355–366.
2. Balletti, C., Guerra, F., Tsiontas, V., & Vernier, P. (2014) Calibration of Action Cameras for Photogrammetric Purposes. *Sensors*, 14(9): 17471-17490; doi:10.3390/s140917471
3. Bay, H., Ess, A., Tuytelaars, T., & Gool, L.V. (2008) SURF: Speeded Up Robust Features. *Comp Vis Image Understanding* 110(3): 346–359.
4. Bradski, G. (2000) The OpenCV Library. Dr. Dobb's Journal of Software Tools. URL: http://docs.opencv.org/doc/tutorials/calib3d/camera_calibration/camera_calibration.html (accessed March 23, 2015).
5. Brisson, J. (2001) Neighborhood competition and crown asymmetry in Acer saccharum. *Can J For Res* 31:2151-2159.
6. Côté, J.-F., Widlowski, J.-L., Fournier, R.A., & Verstraete, M.M. (2009) The structural and radiative consistency of three-dimensional tree reconstructions from terrestrial lidar. *Rem Sens Env* 113(5): 1067–1081.
7. Coulston, J.W., Moisen, G.G., Wilson, B.T., Finco, M.V., Cohen W.B., & Brewer, C.K. (2012) Modeling percent tree canopy cover: a pilot study. *Photogram Eng Rem Sens* 78(7): 715-727.
8. Dandois, J.P., & Ellis, E.C. (2010) Remote sensing of vegetation structure using computer vision. *Rem Sens* 2: 1157–1176.
9. Dandois, J.P., & Ellis, E.C. (2013) High spatial resolution three-dimensional mapping of vegetation spectral dynamics using computer vision. *Rem Sens Env* 136: 259–276.
10. de Matías, J., Sanjosé, J.J. de, López-Nicolás, G., Sagüés, C., & Guerrero, J.J. (2009) Photogrammetric methodology for the production of geomorphologic maps: Application to the Veleta Rock Glacier (Sierra Nevada, Granada, Spain). *Rem Sens* 1: 829–841.
11. Dey, D., Mummert, L., & Sukthankar, R. (2012) Classification of plant structures from uncalibrated image sequences. 2012 IEEE Workshop on Applications of Computer Vision (WACV) pp. 329–336.
12. Erdody, T.L., & Moskal, L.M. (2010) Fusion of LiDAR and imagery for estimating forest canopy fuels. *Rem Sens Env* 114: 725–737.
13. Frelich, L.E. & Martin, G.L. (1988) Effects of crown expansion into gaps on evaluation of disturbance intensity in northern hardwood forests. *For Sci* 34: 530-536.
14. Frew, E.W., Langelaan, J., & Joo, S. (2006) Adaptive receding horizon control for vision-based navigation of small unmanned aircraft. In *Proc IEEE American Control Conference*, 6 pp.
15. Furukawa, Y., & Ponce, J. (2010) Accurate, dense, and robust multiview stereopsis. *IEEE Transactions on Pattern Analysis and Machine Intelligence* 32(8), 1362-1376, DOI 10.1109/TPAMI.2009.161.
16. Gatziolis, D., Fried, J.S., & Monleon, V. (2010) Challenges to estimating tree-height via LiDAR in closed-canopy forests: a parable from western Oregon. *For Sci* 56(2):139-155.
17. Gatziolis, D., Popescu, S.C., Sheridan, R.D., & Ku, N.-W. (2010) Evaluation of terrestrial LiDAR technology for the development of local tree volume equations. Proc. SilviLaser 2010 - The 10th

- International Conference on LiDAR Applications for Assessing Forest Ecosystems, Koch, B., Kändler, G., & Teguem, C. (eds), Freiburg, Germany, 14-17 September, p. 197-205.
18. Gatziolis, D. (2012) Dynamic, LiDAR-based assessment of lighting conditions in Pacific Northwest forests. In *Proceedings of Silvilaser 2012 - The 12th International Conference 'First return'*, p. 16-19.
 19. GDAL (2015). GDAL - Geospatial Data Abstraction Library: Version 1.11.2, Open Source Geospatial Foundation, <http://gdal.osgeo.org>.
 20. Gong, P., Sheng, Y., & Biging, G. (2002) 3D model-based tree measurement from high-resolution aerial imagery. *Photogrammetric Engineering & Remote Sensing*, 68(11): 1203-1212.
 21. Gysel, L.W. (1951) Borders and openings of beech-maple woodlands in southern Michigan. *J For* 49:13-19.
 22. Henning, J.G., & Radtke, P.J. (2006) Detailed stem measurements of standing trees from ground-based scanning Lidar. *For Sci* 52(1): 67-80.
 23. Karaman, S., & Frazzoli, E. (2012) High-speed flight in an ergodic forest. In *Proc Robotics and Automation (ICRA), 2012 IEEE International Conference*, pp. 2899-2906.
 24. Korpela, I., Hovi, A., Morsdorf, F. (2012) Understory trees in airborne LiDAR data — Selective mapping due to transmission losses and echo-triggering mechanisms. *Rem Sens Env* 119: 92–104.
 25. Hirschmugl, M., Ofner, M., Raggam, J., & Schardt, M. (2007) Single tree detection in very high resolution remote sensing data. *Rem Sens Env* 110(4): 533–544.
 26. Leckie, D.G, Gougeon, F.A., Tinis, S., Nelson, T., Burnett, C.N., & Paradine, D. (2005) Automated tree recognition in old growth conifer stands with high resolution digital imagery. *Rem Sens Env* 94(3):311-326.
 27. Levenberg, K. (1944) A method for the solution of certain non-linear problems in least squares. *Quart Appl Math* 2: 164–168.
 28. Levin, S.A. (1999) Fragile dominion: complexity and the commons. Perseus Publishing, Cambridge, MA.
 29. Lindeberg, T. (1998) Feature detection with automatic scale selection. *Int J Comp Vis* 30(2): 79-116.
 30. Loehle, C. (1986) Phototropism of whole trees: Effects of habitat and growth form. *Am Mid Nat* 116: 190-196.
 31. Lowe, D.G. (2004) Distinctive image features from scale-invariant keypoints," *Int J Comp Vis*, 60(2): 91-110.
 32. Maas, H.-G., Bienert, A., Scheller, S., & Keane, E. (2008) Automatic forest inventory parameter determination from terrestrial laser scanner data. *Int J Rem Sens* 29(5): 1579-1593, DOI: 10.1080/01431160701736406
 33. Marquardt D. (1963). An algorithm for least-squares estimation of nonlinear parameters. *SIAM J Appl Math* 11(2): 431–441 doi:10.1137/0111030.
 34. Metz., J., Seidel, D., Schall, P., Scheffer, D., Schulze E.-D., & Ammera, C. (2013) Crown modeling by terrestrial laser scanning as an approach to assess the effect of aboveground intra- and interspecific competition on tree growth. *Forest Ecol Manag* 310: 275–288.

35. Mori, T., & Scherer, S. (2013) First results in detecting and avoiding frontal obstacles from a monocular camera for micro unmanned aerial vehicles. In *Proc Robotics and Automation (ICRA), 2013 IEEE International Conference*, pp. 1750-1757.
36. Munro, D.D. (1974) Forest Growth Models: A Prognosis, in Fries, J. (ed.), *Growth Models for Tree and Stand Simulation*, Dept. of Forest Yield Research, Royal College of Forestry, Stockholm, Res. Notes Vol. 30.
37. Popescu, S.C., Wynne, R.H., & Nelson, R.F. (2003) Measuring individual tree crown diameter with lidar and assessing its influence on estimating forest volume and biomass *Can J Rem Sens* 29(5): 564–577.
38. Popescu, S.C., Zhao, K. (2008) A voxel-based lidar method for estimating crown base height for deciduous and pine trees. *Rem Sens Env* 112(3): 767-781.
39. Reda, I., & Andreas, A. 2008. Solar Position Algorithm for Solar Radiation Applications. Technical Report NREL/TP-560-34302, National Renewable Energy Laboratory, Golden, Colorado, 56 pp.
40. Roberts, R., Ta, D.-N., Straub, J., Ok, K., & Dellaert, F. (2012) Saliency detection and model-based tracking: a two part vision system for small robot navigation in forested environment. In *Proc SPIE 8387, Unmanned Systems Technology XIV*; DOI 10.1117/12.919598, pp 12.
41. Rothermel, M., Wenzel, K., Fritsch, D., & Haala, N. (2012) SURE: Photogrammetric Surface Reconstruction from Imagery. In *Proc LC3D Workshop*, Berlin Germany, December 2012.
42. Rosnell, T., & Honkavaara, E. (2012) Point cloud generation from aerial image data acquired by a quadrocopter type micro unmanned aerial vehicle and a digital still camera. *Sensors*, 12: 453–480.
43. Ross, S., Melik-Barkhudarov, N., Shankar, K.Sh., Wendel, A., Dey, D., Bagnell, J.A., & Hebert, M. (2013) Learning monocular reactive UAV control in cluttered natural environments. In *Proc Robotics and Automation (ICRA), 2013 IEEE International Conference on*, pp. 1765-1772.
44. Rublee, E., Rabaud, V., Konolige, K., & Bradski, G. (2011). ORB: an efficient alternative to SIFT or SURF. In *Computer Vision (ICCV), 2011 IEEE International Conference on Computer Vision (ICCV)*, pp. 2564-2571, DOI: 10.1109/ICCV.2011.6126544.
45. Sheridan, R.D., Popescu, S.C., Gatzilis, D., Morgan, C.L.S., & Ku, N-W. (2015) Modeling forest aboveground biomass and volume using airborne LiDAR metrics and Forest Inventory and Analysis data in the Pacific Northwest. *Rem Sens* 7:229-255.
46. Shreiner, D. (2009) OpenGL programming guide: The official guide to learning OpenGL, versions 3.0 and 3.1 (7th ed.). Addison-Wesley Professional.
47. Skurikhin, A.N., Garrity, S.R., McDowell N.G., & Cai, D.M. (2013) Automated tree crown detection and size estimation using multi-scale analysis of high-resolution satellite imagery. *Rem Sens Lett* 4(5):465-474, DOI: 10.1080/2150704X.2012.749361
48. Snavely, N., Seitz, S., & Szeliski, R. (2008) Modeling the world from internet photo collections. *Int J Comp Vis* 80: 189–210.
49. Song, C. (2007) Estimating tree crown size with spatial information of high resolution optical remotely sensed imagery. *Int J Rem Sens* 28(15): 3305-3322, DOI: 10.1080/01431160600993413
50. Stoll, P., & Schmid, B. (1998) Plant foraging and dynamic competition between branches of *Pinus sylvestris* in contrasting light environments. *J Ecol* 86:934-945.

51. Strigul, N.S. (2012) Individual-Based Models and Scaling Methods for Ecological Forestry: Implications of Tree Phenotypic Plasticity, Sustainable Forest Management, Dr. Julio J. Diez (Ed.), InTech, Croatia
52. Strigul, N.S., Pristinski, D., Purves, D., Dushoff, J., & Pacala, S.W. (2008). Scaling from trees to forests: Tractable macroscopic equations for forest dynamics. *Ecol Monogr* 78:523-545.
53. Umeki, K. (1995) A comparison of crown asymmetry between *Picea abies* and *Betula maximowicziana*. *Can J For Res* 25:1876-1880.
54. Webster, C.R., & Lorimer, C.G. (2005) Minimum opening sizes for canopy recruitment of midtolerant tree species: A retrospective approach. *Ecol Appl* 15:1245-1262.
55. Woods, F.W., & Shanks, R.E. (1959) Natural replacement of chestnut by other species in the Great Smoky Mountains National Park. *Ecology* 40:349-361.
56. Wu, C. (2013) Towards linear-time incremental structure from motion. In *Proc 2013 IEEE International Conference on 3D Vision-3DV*, pp 127-134.
57. Wu, C. (2014) Critical configurations for radial distortion self-calibration. In *Proc IEEE Conference on Computer Vision and Pattern Recognition*, New York.
58. Wu, C., Agarwal, S., Curless, B., & Seitz, S. M. (2011) Multicore bundle adjustment. In *Proc 2011 IEEE Conference on Computer Vision and Pattern Recognition (CVPR)*, pp. 3057-3064.
59. Wulder, M., Niemann, K.O., & Goodenough, D.G. (2000) Local maximum filtering for the extraction of tree locations and basal area from high spatial resolution imagery. *Rem Sens Env* 73:103–114.
60. Young, T.P., & Hubbell, S.P. (1991) Crown asymmetry, tree falls, and repeat disturbance in a broad-leaved forest. *Ecology* 72:1464-1471.
61. Zhang, Z., Deriche, R., Faugeras, O., & Luong, Q.-T. (1995) A robust technique for matching two uncalibrated images through the recovery of the unknown epipolar geometry. *Artificial Intelligence* 78(1-2):87-119 DOI 10.1016/0004-3702(95)00022-4
62. Zhao, K., Popescu, S.C., & Nelson, R.F. (2009). Lidar remote sensing of forest biomass: A scale-invariant estimation approach using airborne lasers. *Rem Sens Env* 113(1):182-196.

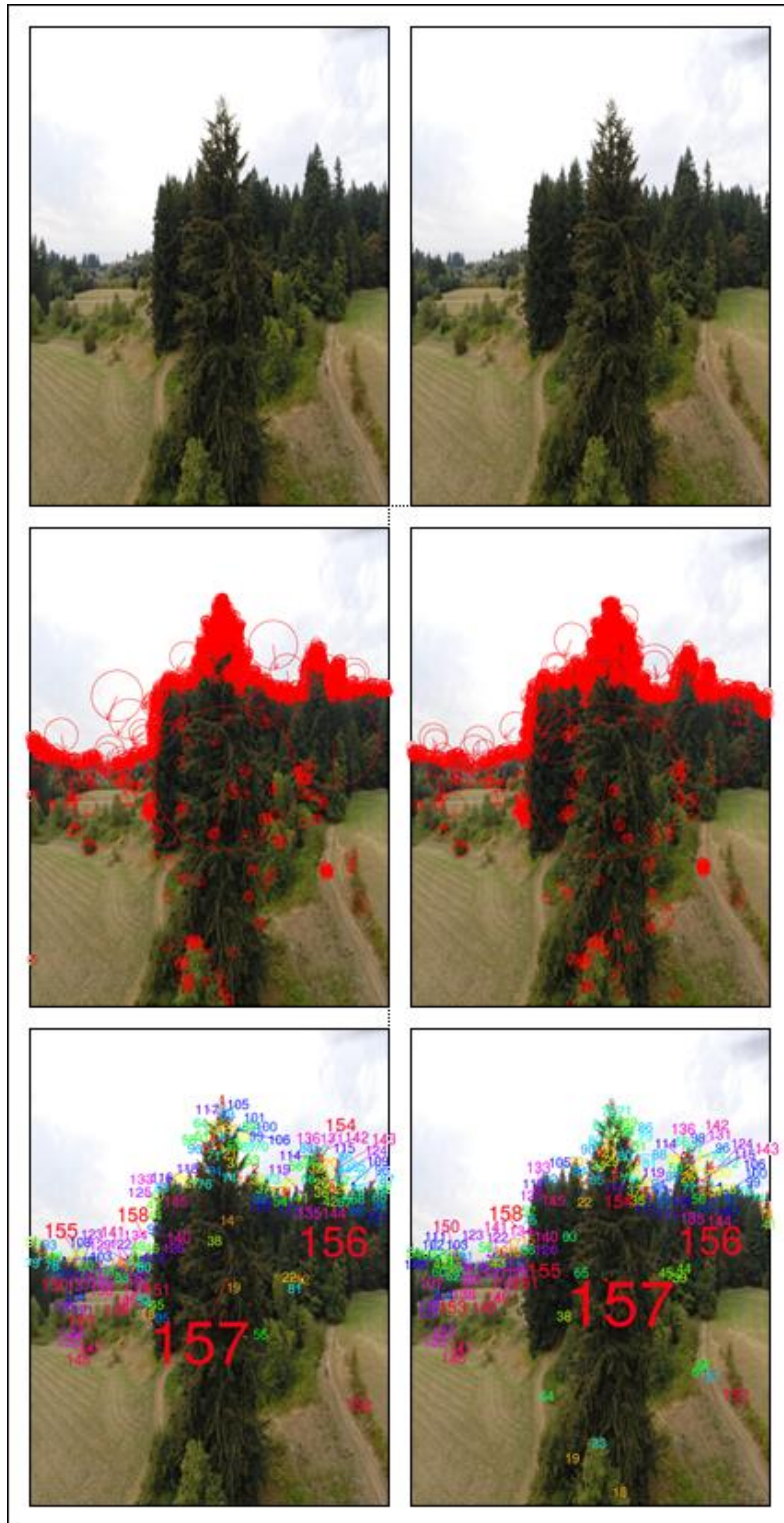


Figure 1. SIFT-based scene keypoint detection and matching on two overlapping images.
Top: Original images; Middle: 1464 (left) and 1477 (right) keypoints with arrows denoting orientation and radii scale; Bottom: 157 keypoint pairs, matched by color and number.



Figure 2. Removal of lens distortion.

Demonstration of a. original, vs. b. OpenCV-calibrated lateral tree image obtained with a UAV-based GoPro camera at an above-ground altitude of 18 meters. Horizontal red line drawn to illustrate form of horizon in each version of the image.

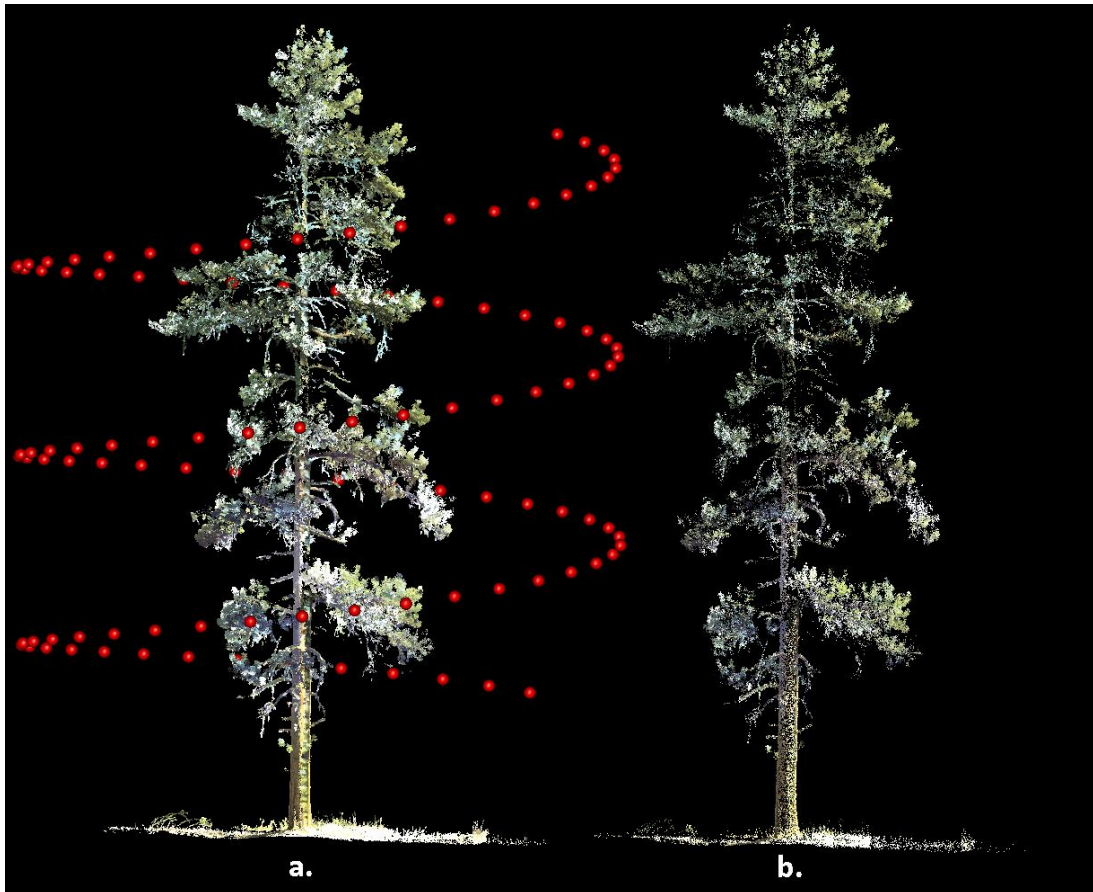


Figure 3. 3D reconstruction in simulation.

a. Perspective view of point cloud acquired with terrestrial LiDAR and camera locations (red spheres) used to obtain virtual images of the scene. b. Scene reconstruction obtained by processing of the images.



Figure 4. Custom built UAV hexacopter used to collect imagery data in this study.

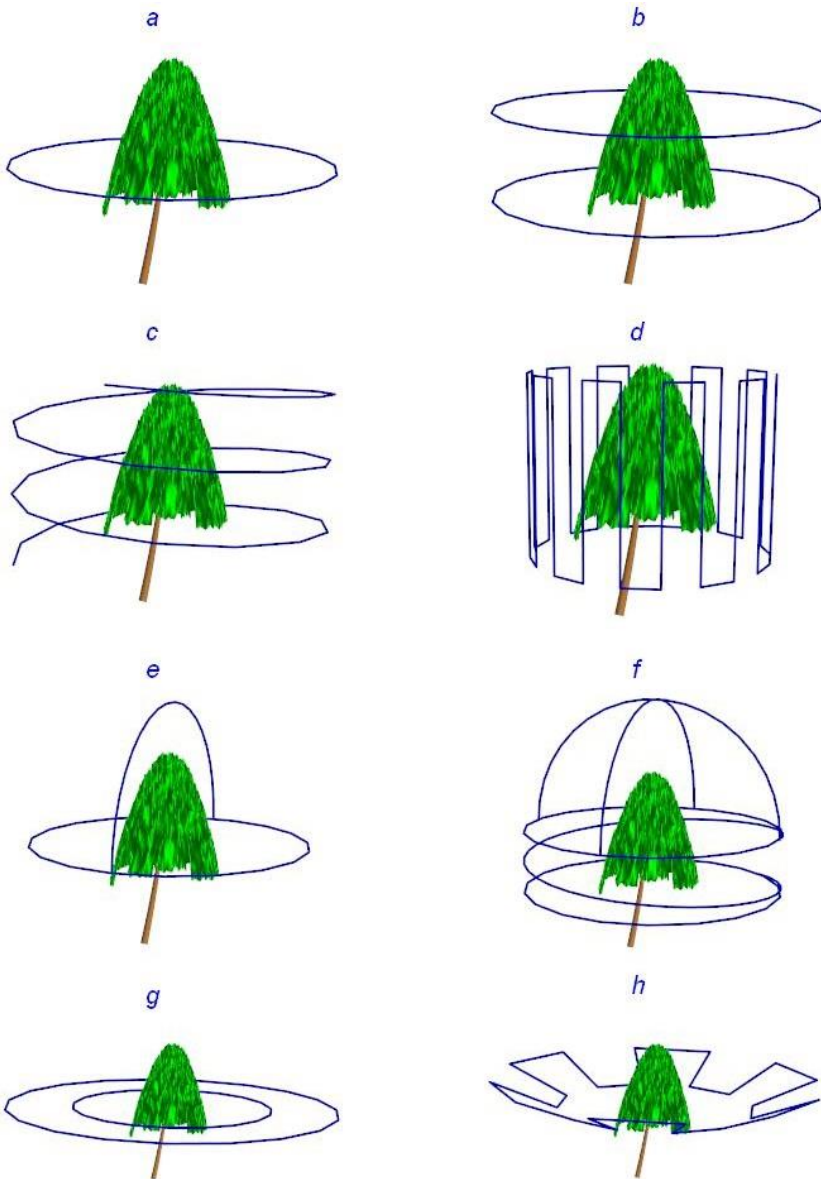


Figure 5. Different UAV trajectories tested for image acquisition.

a. circular, at constant height; *b.* 'stacked circles', each at different above-ground height, for tall trees (height more than 20 m); *c.* spiral, for trees with complex geometry; *d.* vertical meandering, targeting tree sectors; *e.* clover, for trees with wide, ellipsoidal tree crowns; *f.* 'spring-hemisphere', designed for trees with flat-top, asymmetrical crowns; *g.* 'nested circles', centered on the tree; and *h.* 'jagged saucer', designed for trees with dense foliage but low crown compaction ratio.

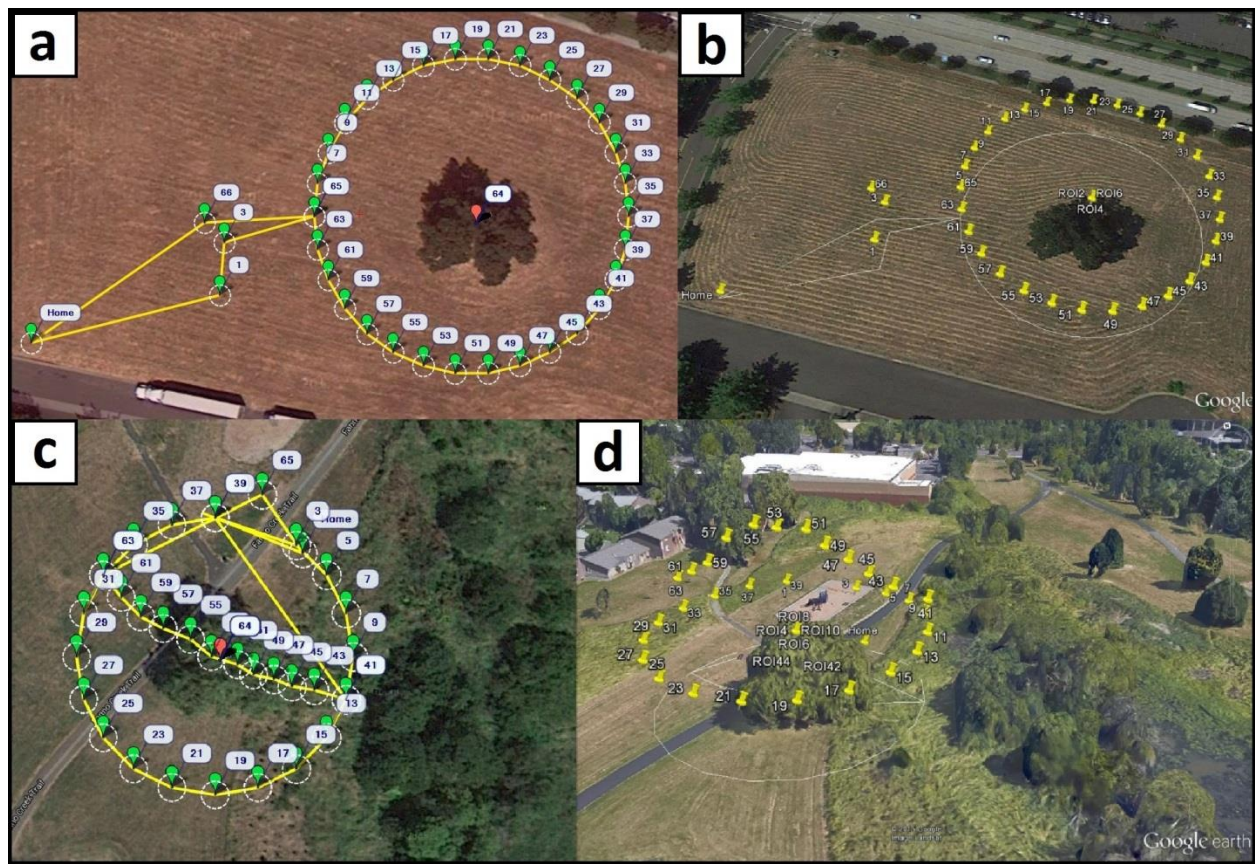


Figure 6. Visualization of designed and accomplished UAV trajectories.

a. and c. circular and clover templates as seen in Mission Planner with yellow lines showing the flight paths, green balloons indicating waypoints, and red balloons the center of targeted trees. b. and d. perspective scene view in Google Earth, with yellow pins indicating camera locations along each trajectory at the moment images were captured.

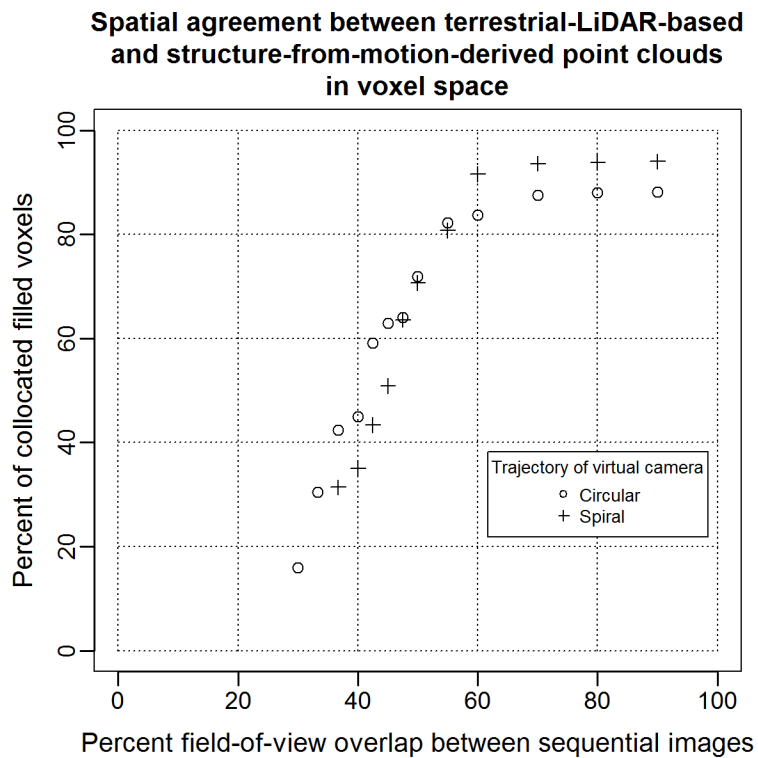


Figure 7. Accuracy and completeness of reconstruction for a *Pinus ponderosa* tree.

This analysis is based on synthetic imagery simulated using visualization of terrestrial LiDAR point clouds and two camera trajectories. Percentage of collocated filled voxels is used as reconstruction completeness criterion.



Figure 8. Orthographic horizontal view of reconstructed point cloud and UAV-based oblique perspective image. Colored arrows denote corresponding tree crown components.

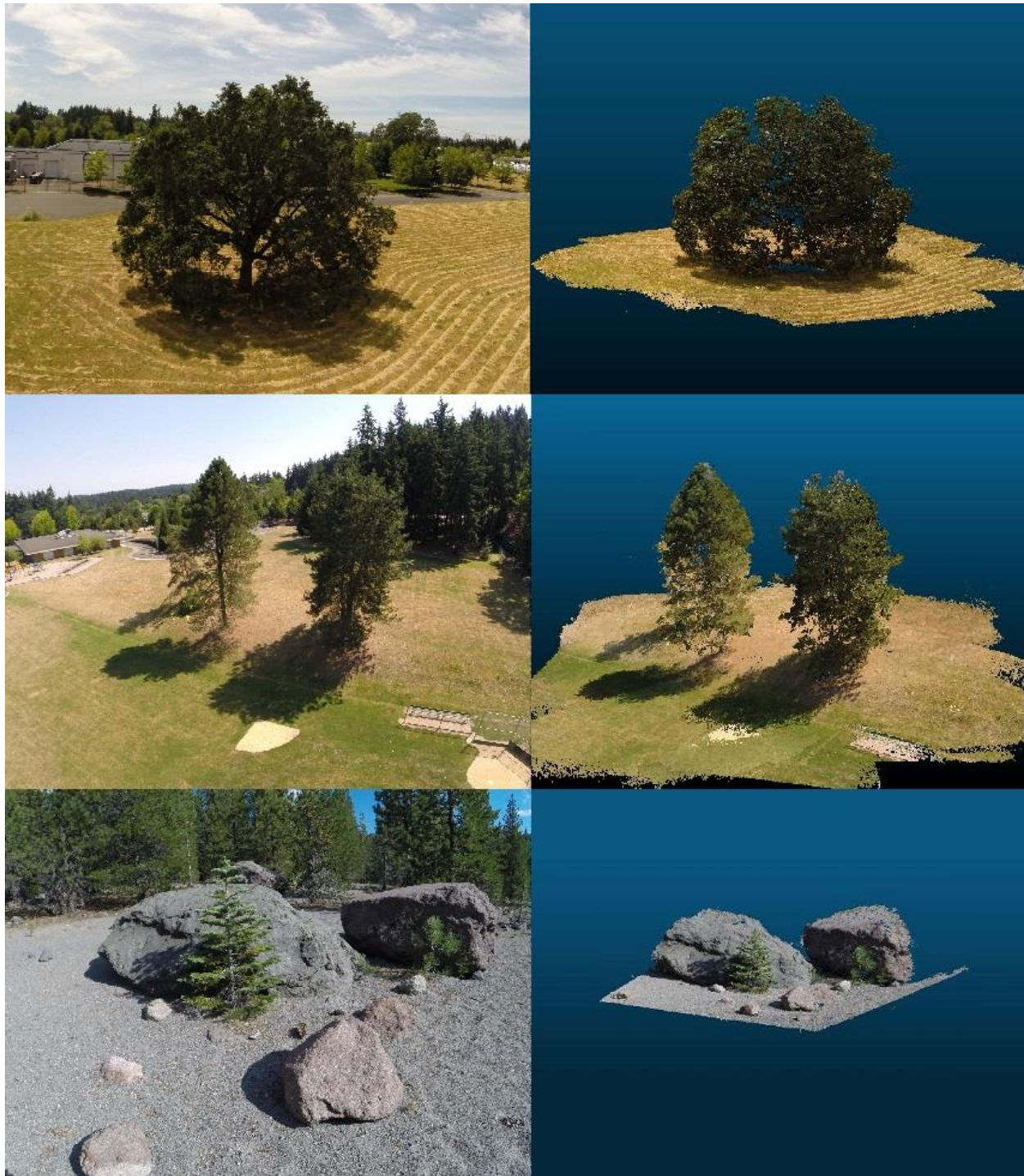


Figure 9. Illustration of comprehensive tree reconstructions (right column) and reference UAV-based images (left column).

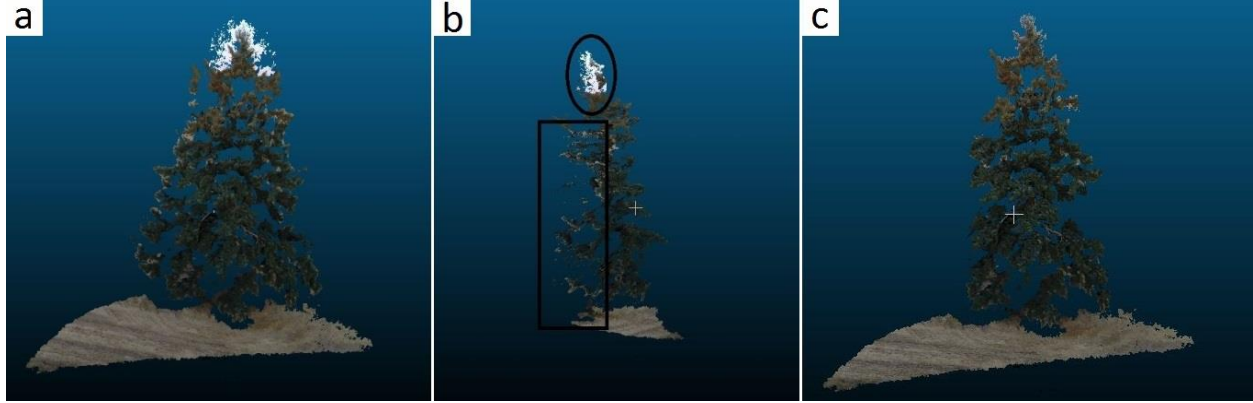


Figure 10. Demonstration of artifacts in the 3D tree reconstruction pertaining to a single UAV image.
a. Initial reconstruction, positioned facing the camera with a band of white-colored points belonging to sky background near the top, and light colored points to the sides belonging to fallow land background,
b. Side view, with camera position to the left and sky points in oval and land points in rectangle, and c. Trimmed reconstruction positioned facing the camera.

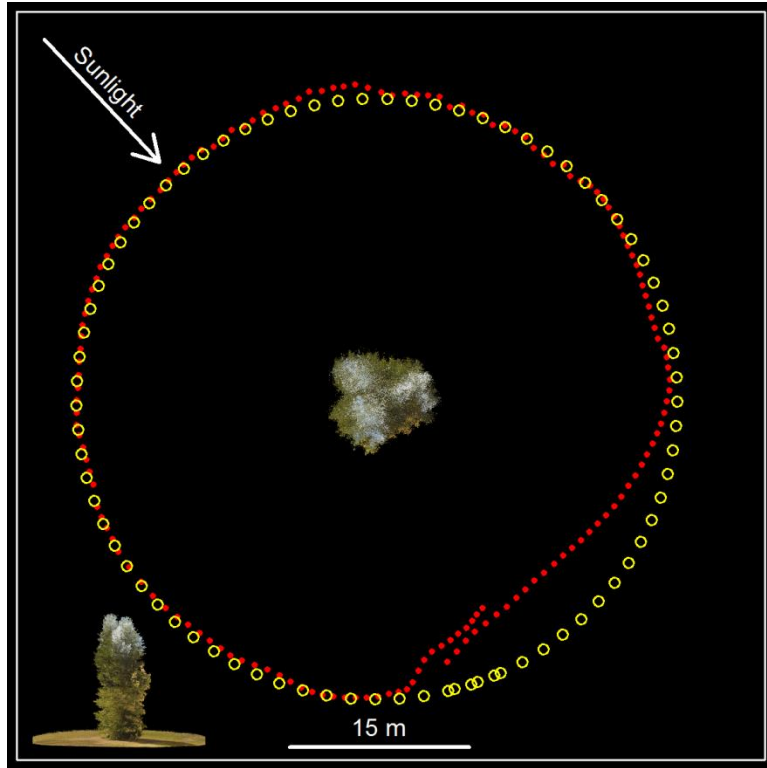


Figure 11. Comparison between real and reconstructed trajectory. Nadir view of reconstructed tree with camera GPS locations at image frame acquisition moments (yellow circles) and VSfM-calculated locations (red dots). Frame frequency 2Hz, GPS fixes at 1Hz. Inset at the lower left shows lateral view of the reconstructed tree.